

Visible-frequency hyperbolic plasmon polaritons in a natural van der Waals crystal

Received: 15 October 2024

Accepted: 30 October 2024

Published online: 10 November 2024

Giacomo Venturi^{1,2,3}, Andrea Mancini^{1,3}  , Nicola Melchioni^{1,3}, Stefano Chiodini¹ & Antonio Ambrosio¹  

Controlling light at subwavelength scales is crucial in nanophotonics. Hyperbolic polaritons, supporting arbitrarily large wavevectors, enable extreme light confinement beyond the diffraction limit. Traditional hyperbolic metamaterials suffer from high losses due to metallic components, while natural low-loss hyperbolic phonon polaritons are limited to the mid-infrared range. Some hyperbolic materials at visible frequencies have been studied, but they are either very lossy or only feature out-of-plane hyperbolicity. Here, we demonstrate the presence of low-loss, in-plane hyperbolic plasmon polaritons in the visible and near-infrared in thin-films of MoOCl₂, a natural van der Waals crystal. The polariton dispersion is predicted based on the framework of light propagation in biaxial media and experimentally confirmed by real space nano imaging on exfoliated flakes. MoOCl₂ constitutes an ideal material platform for visible range applications leveraging the unboundedness of hyperbolic modes, such as hyperlensing, Purcell factor enhancement, and super-resolution imaging, without the drawbacks of metamaterials.


In the past decade, polaritons¹ - mixed light-matter states formed by coupling photons with quantum excitations of crystals (e.g. optical phonons or plasmons) - have enabled the control of light at the sub-wavelength scale, emerging as game changers for several applications encompassing nanoscale heat generation^{2,3}, photocatalysis^{4,5}, enhanced surface spectroscopies^{6,7}, wavefront engineering⁸⁻¹⁰ and nonlinear optics^{11,12}.

The confinement provided by polaritons is determined by the material dielectric permittivity and described by the isofrequency contours (IFCs) defining the allowed wavevectors for propagating modes at a certain wavelength. When the permittivity tensor is diagonal with all negative components, polaritons propagate at the material boundary with spherical or elliptic wavefronts, associated with closed IFCs (Fig. 1a). Conversely, anisotropic materials with a permittivity that is negative (i.e., metallic-like) and positive (i.e., dielectric-like) along orthogonal directions support polaritons with hyperbolic wavefronts, defined by strongly anisotropic IFCs featuring arbitrarily large wavevectors (Fig. 1b)^{13,14}. Thus, as the wavelength is inversely

proportional to the wavevector, hyperbolic polaritons can be leveraged to confine light at extremely subwavelength scales^{15,16}.

A versatile platform for polaritonics is provided by van der Waals (vdW) materials¹, such as hexagonal boron nitride (hBN)¹⁷⁻²¹, α -MoO₃^{22,23} and β -Ga₂O₃^{24,25}, recently shown to support hyperbolic phonon polaritons (PhPs). Their highly anisotropic lattice results in different phonon resonances along each crystal direction, causing the permittivity tensor elements to have opposite signs at mid-infrared (IR) frequencies (Fig. 1c). Exploiting the hyperbolic IFCs, highly controlled unidirectional²⁶ and canalized²⁷ PhPs propagation, as well as negative reflection²⁸ and refraction²⁹ have been recently demonstrated. While PhPs are promising for applications in thermal radiation engineering³⁰ and vibrational sensing³¹, highly sought implementations for hyperlensing³², enhanced quantum emission³³, super-resolution imaging³⁴, and high-resolution photolithography³⁵ require operation in the visible range. As PhPs are limited to IR wavelengths ($\lambda_0 > 5 \mu\text{m}$) due to the characteristic energy of optical phonons, exploring alternative platforms is essential.

¹Centre for Nano Science and Technology, Fondazione Istituto Italiano di Tecnologia, Milano, Italy. ²Physics Department, Politecnico di Milano, Milano, Italy.

³These authors contributed equally: Giacomo Venturi, Andrea Mancini, Nicola Melchioni.  e-mail: andrea.mancini@iit.it; antonio.ambrosio@iit.it

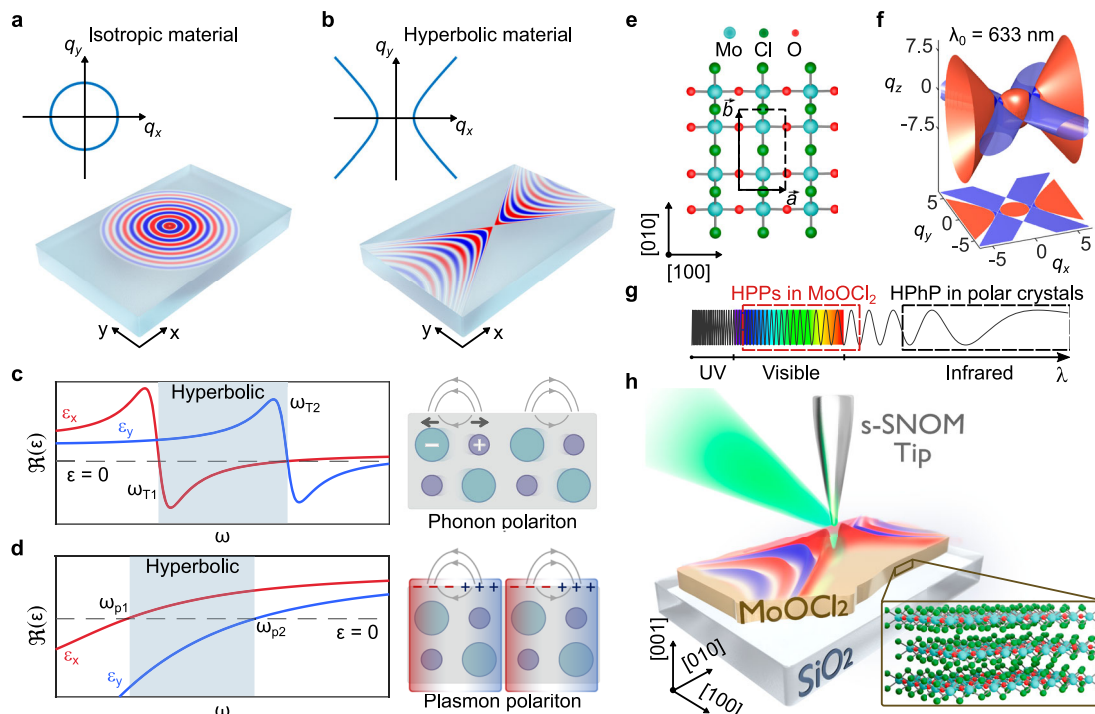


Fig. 1 | Hyperbolic plasmon polaritons at visible frequencies. **a** Polaritons in isotropic materials propagate with circular wavefronts with in-plane momenta q_x , q_y (in units of the free-space wavevector), associated with closed isofrequency contours (IFCs, inset). **b** Polaritons in hyperbolic materials propagate with hyperbolic wavefronts set by the unbounded IFCs (inset). **c** Different (optical) phonon resonances (ω_{T1} , ω_{T2}) cause the dielectric permittivity ϵ to be negative in one direction, defining a hyperbolic spectral region (grey shaded area, left panel) in which phonon polaritons (PhPs) are formed (right panel). **d** Different plasma frequencies (ω_{p1} , ω_{p2}) give rise to hyperbolic windows (grey shaded area, left panel),

where light couples to quasi-free electrons forming plasmon polaritons (PPs, right panel). **e** In-plane crystal structure of MoOCl_2 , where q_z is the (normalized) out-of-plane wavevector. 2D unit cell vectors are shown. **f** IFCs of bulk MoOCl_2 computed for $\lambda_0 = 633$ nm. **g** Hyperbolic PhPs lie in the IR region due to the limited energy of phonons. Hyperbolic PPs in MoOCl_2 , instead, span a large portion of the visible and near IR. **h** MoOCl_2 PPs can be imaged with scattering-type scanning near field optical microscope (s-SNOM), consisting of a metallic tip illuminated by (visible) light. The scattered near-field provides the high momenta required to excite sub-diffraction polaritons. Inset: crystal structure of bulk MoOCl_2 .

Operation at visible frequencies has been realized with nanostructured hybrid metal-dielectric materials, called metamaterials, which can be tailored to show hyperbolic plasmon polaritons (PPs)¹⁴. Even though negative refraction³⁶ and hyperlensing^{32,37} have been demonstrated with hyperbolic metamaterials in the visible, such artificial materials are constrained by the limited fabrication resolution of lithography processes and can only work in the long wavelength limit for which the effective medium approximation holds¹⁴, thus hindering their operation at large momenta. Moreover, the presence of noble metals in the metamaterial structure makes them typically very lossy at visible frequencies.

Natural hyperbolic materials can help circumvent such limitations. Hyperbolicity in the visible range has been found originating from anisotropic excitons^{38,39}, interband transitions⁴⁰, plasmons (Fig. 1d)^{41,42}, or a combination of them^{43,44}. However, until now either the presence of high losses or the out-of-plane nature of the response prevented the observation of natural hyperbolic polaritons in the visible. Only recently, near-IR real space nanoimaging of hyperbolic exciton polaritons has been reported in CrSBr thin-films⁴⁵, but only at cryogenic temperatures. Moreover, their coexistence with waveguide modes hampered their visualization. As a result, no clear evidence of room temperature in-plane hyperbolic polaritons in the visible range has been reported so far.

In this work, we report the discovery of low-loss in-plane hyperbolic plasmon polaritons at visible and near-IR frequencies in thin-films of the natural vdW crystal molybdenum oxide dichloride (MoOCl_2), whose in-plane crystal structure is sketched in Fig. 1e. First, we give a description of the PPs supported by bulk MoOCl_2 in the theoretical

framework of polariton propagation in biaxial media. Our analysis reveals the simultaneous presence of hyperbolic PPs as well as directional ghost modes in the material (i.e., modes showing damped propagation even in the absence of material losses)⁴⁶, as represented by the IFCs in Fig. 1f. Thanks to the broad hyperbolic region of MoOCl_2 , these modes span the near-IR and visible ranges (Fig. 1g). We then discuss the modification of the PPs IFCs from the bulk to the thin-film limit. We experimentally confirm the optical anisotropy of MoOCl_2 through high-resolution atomic force microscopy and far-field reflectivity. Finally, we investigate the predicted thin-film IFCs through real space polariton nanoimaging on exfoliated MoOCl_2 (as illustrated in Fig. 1h). Our demonstration of low-loss in-plane natural hyperbolicity in the visible range paves the way for enhanced control of light confinement through the unboundedness of polariton IFCs, with promising applications in high-frequency 2D materials-based optoelectronics.

Results

Plasmon polaritons in bulk MoOCl_2

MoOCl_2 is a layered vdW material belonging to the subgroup of oxychlorides with formula XOCl_2 (X = Mo, Nb, Ta, V, Os), whose crystal structure is characterized by a monoclinic lattice (space group $C2/m$)^{47,48}. The structure of a single layer of the MoOCl_2 crystal consists of a central plane made of Mo-O chains (extending in the [100] direction) sandwiched between two layers of Cl atoms as shown in the inset of Fig. 1h⁴⁹. The in-plane lattice takes a rectangular shape (Fig. 1e), with orthogonal unit cell vectors \mathbf{a} , \mathbf{b} with sizes 3.8 Å and 6.5 Å⁴⁹, respectively. Monolayers are stacked in the [001] direction at a distance of 12.7 Å to form the bulk.

Recent theoretical works derived the optical constants of biaxial MoOCl₂^{47,48}. The calculated dielectric tensor is diagonal with three different principal components ($\epsilon_x, \epsilon_y, \epsilon_z$) (here we associate the (x, y, z) directions with the crystalline axes [100], [010] and [001]). A broad hyperbolic region across the near-IR and visible ranges where $\epsilon_x < 0$ and $\epsilon_y, \epsilon_z > 0$ is expected, originating from a metallic character with highly different values for the plasma frequency (ω_p) along distinct crystalline directions (as sketched in Fig. 1d; for details refer to Supplementary Note 1). Intuitively, this is a result of the Mo-O atoms behaving as isolated chains due to their much stronger lattice binding compared to the other crystal directions⁴⁷. The MoOCl₂ hyperbolic region is also predicted to be low-loss⁴⁸ (see Supplementary Note 1), suggesting the possibility of observing the propagation of hyperbolic PPs.

Based on the theoretical values of the MoOCl₂ optical constants, we calculate its IFCs at $\lambda_0 = 633$ nm in the hyperbolic spectral range (Fig. 1f, where $\mathbf{q} = (q_x, q_y, q_z)$ is the normalized wavevector; see Supplementary Note 2)⁵⁰. The orange IFCs show the coexistence of hyperbolic modes with unbounded wavevectors in the q_x direction, alongside a central spheroidal region resembling the IFC of a dielectric material. Furthermore, our calculations predict the existence of directional ghost modes (light purple)^{46,51}.

Ghost modes are an exotic class of waves featuring damped propagation with a complex wavevector even in the absence of intrinsic material losses⁵¹. To investigate the presence of ghost modes it is therefore instructive to inspect the in-plane projections of the real (left) and imaginary (right) parts of the analytically derived IFCs shown in Fig. 2a ($\lambda_0 = 633$ nm). In the (q_x, q_y) space, three distinct domains can be observed as delimited by the black continuous, dashed, and dotted lines, corresponding to three different propagating modes. Spherical-like waves exist within the dotted circle, whose radius is determined by the out-of-plane refractive index of MoOCl₂ ($|\mathbf{q}| = n_z$). The continuous curves delimit the hyperbolic regions asymptotically approaching

straight lines defined by $q_y/q_x = \pm \sqrt{-\epsilon_x/\epsilon_y}$. The dashed lines delimit the region in momentum space where ghost modes exist, as this is the only part of the IFCs where at the same time both the real and imaginary part of q_z are nonzero (even when the material is lossless)⁵¹. Similarly to hyperbolic PPs, ghost PPs are highly confined as their IFCs are unbounded. Ghost PPs are also strongly directional as defined by the angular coefficient of the straight IFCs boundaries $q_y/q_x = \pm \sqrt{(\epsilon_x - \epsilon_z)/(\epsilon_y - \epsilon_z)}$ ⁵¹. Remarkably, ghost modes in MoOCl₂ are fundamentally different from the ones recently observed in calcite⁴⁶. In this latter case, ghost modes appear as surface waves at the boundary between an off-cut uniaxial crystal and a dielectric, and feature in-plane hyperbolic dispersion. In MoOCl₂, ghost waves are intrinsic bulk modes of a biaxial crystal, without the need of an interface with an off-axis cut. Their existence only depends on the relative magnitude of the dielectric tensor components (see Supplementary Note 2 for more details) and they do not feature hyperbolic dispersion. They rather populate a cross-shaped region in momentum space (see Fig. 2a, b).

To verify the prediction of the analytical calculations, we perform three-dimensional full-wave electromagnetic simulations at $\lambda_0 = 633$ nm, the same free-space wavelength of the computed theoretical IFCs of Figs. 1e and 2a, b. The thickness of the slab is chosen so that there is no appreciable interaction between the polaritons and the top/bottom interfaces, effectively approximating the behaviour of an infinite crystal. By cutting the simulated $\text{Re}(E_z)$ field distribution along orthogonal planes (Fig. 2c), we observe the expected propagation of hyperbolic PPs in the x direction (x - z cut), whereas along y spherical wavefronts are in line with the dipolar emission in a dielectric environment (y - z cut). The propagation direction for the observed PPs is determined by the Poynting vector, which is perpendicular to the IFCs⁵². For ghost waves, the angular coefficient of the straight lines defining the region of ghost modes is 54° at $\lambda_0 = 633$ nm (dashed lines in Fig. 2a), yielding a predicted in-plane propagation direction of

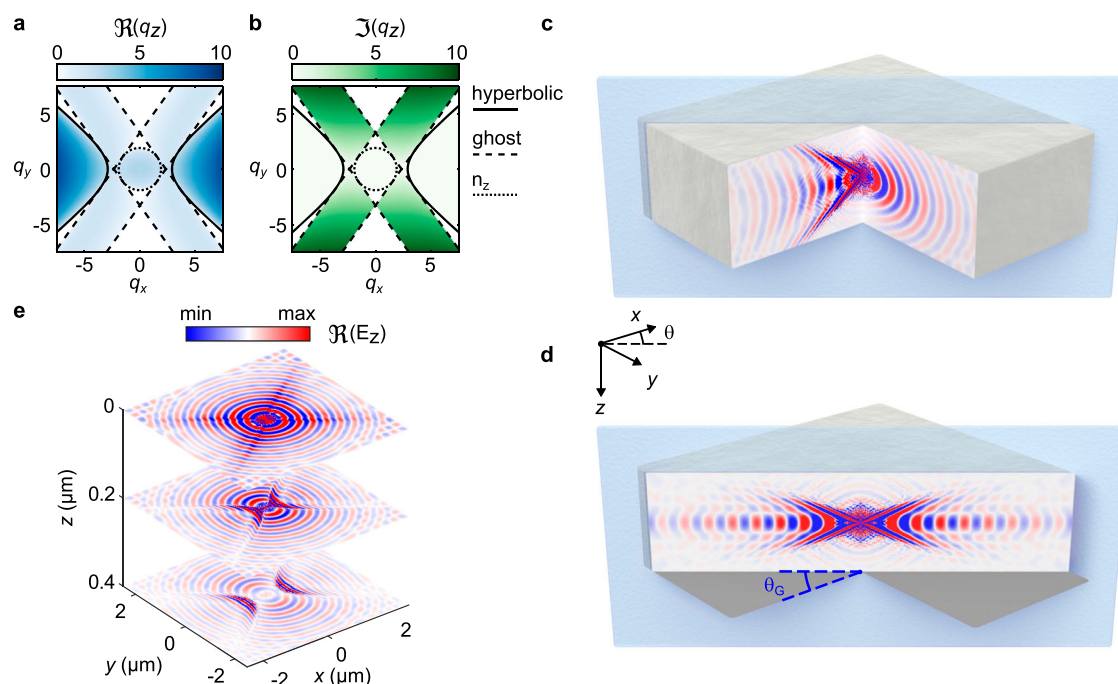


Fig. 2 | Anisotropic plasmon polaritons propagation in bulk MoOCl₂. **a** In-plane projection of the real and **b** imaginary (right) parts of the calculated IFCs ($\lambda_0 = 633$ nm, without material losses). Solid and dashed lines delimit the boundaries of the hyperbolic and ghost propagating regions. Dotted line corresponds to the $|\mathbf{q}| = n_z$ circle (i.e., MoOCl₂ light-cone, where n_z is the out-of-plane refractive index). **c, d** Three-dimensional full-wave simulations of PPs emitted by a near-field source

located in the middle of a slab of MoOCl₂ ($1.5 \mu\text{m}$ thickness). **c** Projections of the out-of-plane electric field E_z field on the x - z and y - z planes and **d** on the y - z plane rotated clockwise by $\theta_G = 36^\circ$ around the z -axis, aligned with the directional propagation of ghost PPs. **e** In-plane values of the simulated E_z field at different distances from the near-field source.

$\theta_G = 36^\circ$ in real-space. The fields evaluated in a plane rotated by $\approx \theta_G$ with respect to the x - z plane (Fig. 2d) show the existence of highly directional PPs confined both in z and in the θ_G -oriented plane, which we identify with the ghost modes predicted by our theoretical analysis (see Supplementary Note 2).

In the θ_G cut (Fig. 2d), we also observe the presence of hyperbolic PPs with a smaller out-of-plane opening angle compared to the ones appearing in the $x - z$ cut (Fig. 2c). This effect is explained by considering the direction of the Poynting vector in relation to the orientation of the cut plane (see Supplementary Note 2).

The properties of PPs can be also visualized from the in-plane projections of $\text{Re}(E_z)$ at three different depths (0, 200 and 400 nm away from the near-field source plane, located at the centre of the slab) shown in Fig. 2e. Ghost PPs are confined at $z = 0$ and are canalized along four specific directions⁵³. An almost isotropic emission (equal along x and y , but different along z) associated with dielectric modes (central spheroid in the IFCs of Fig. 1f) is also present in the simulations, which interferes with both hyperbolic and ghost PPs.

Plasmon polaritons in MoOCl₂ thin-films

Having described the bulk modes, we move to the analysis of PPs in thin-films. As recently shown for hBN¹⁷ and MoO₃²³, bulk hyperbolic polaritons get reflected at the material's top and bottom interfaces, as sketched in Fig. 3a, forming waveguide-like modes propagating inside the flake (see Supplementary Note 5). To better understand how the modes evolve with the film thickness, we report in Fig. 3b the in-plane dispersion calculated through the transfer matrix method for four different thicknesses between 80 nm and 20 nm. At 80 nm we observe two hyperbolic modes (symmetric with respect to the q_y axis), lying outside the substrate isotropic light-cone, with two different apertures: the lowest order bulk mode, with higher wavevectors, and a mode with smaller curvature, only visible for thicknesses below ~ 200 nm (see Supplementary Note 5). The hyperbola of the latter does not actually close at its vertex and its intensity drops to zero for $q_x < n_z$. In this region, the IFCs change from a hyperbolic to a lenticular-like dispersion, in a similar fashion to reported cases of mid-IR surface PhPs modes⁵³. Such a transition in the mode shape when crossing n_z can be better appreciated for a 40 nm-thick film, shown in the inset of Fig. 3b. By further reducing the thickness, the vertex of the hyperbola lies completely outside of the n_z circle and the lenticular mode disappears as shown in the dispersion for the 20 nm-thick film. Lenticular modes in MoOCl₂ share some features with leaky modes observed in calcite: both are characterized by lenticular-shaped IFCs and can be excited within the material light cone ($q < n_z$) as long as one in-plane tensor component is negative, while the other two are positive (this is possible in both uniaxial and biaxial crystals). However, leaky modes in calcite are interface waves in semi-infinite uniaxial slabs, while the lenticular modes predicted in MoOCl₂ appear as waves solutions for a biaxial thin-film and exist outside the light cone of the substrate ($n_z > q > n_{sub}$).

In Fig. 3c we report numerical full-wave simulations of the E_z field in a 40 nm film produced by a dipole placed just above the MoOCl₂ layer, which shows the excitation of mainly hyperbolic-like PPs. Nevertheless, the (fast-)Fourier transform (FFT) map of the calculated field in Fig. 3d confirms the existence of both the hyperbolic and lenticular PPs predicted by the transfer matrix. To have a further confirmation, we use the recently developed analytical expression for polariton dispersion in biaxial media^{50,51} in the small thickness limit ($\kappa_0 d \ll 1$, $\kappa_0 = 2\pi/\lambda_0$) to extract the theoretical PPs dispersions (see Supplementary Note 2). The analytical solution for the PPs, shown as solid lines in Fig. 3d, confirms again the coexistence of a hyperbolic (green) and a lenticular (red) dispersion (blue line indicates the $n_{sub} = 1.5$ contour). While lenticular modes have been observed in semi-infinite calcite slabs, their existence as thin-film solutions in MoOCl₂

enables the observation of their unique interference with hyperbolic modes.

Real-space imaging of thin-film hyperbolic plasmon polaritons
In the following, we experimentally confirm the presence of the predicted hyperbolic PPs by real space nano-imaging.

Thin flakes were obtained by mechanical exfoliation of commercially available bulk MoOCl₂ on 285 nm SiO₂/Si substrates (see Methods). A representative flake seen under the optical microscope is shown in Fig. 4a. Since there is no experimental data in literature about the optical properties of the material, we first look for a confirmation of the anisotropic optical response of the as-exfoliated material. Figure 4a shows remarkably different flake colours when placing a polarizer in the illumination path, aligned with either the short (left) or long (right) edge of the flake (see Methods). This, in combination with the rectangular shape of the exfoliated flakes (which we observe over many samples, see Supplementary Note 3), suggests that MoOCl₂ naturally breaks along the [100] and [010] directions. To provide a direct confirmation of such hypothesis, we perform atomic-resolution atomic force microscopy (AFM, see Methods) of the flake surface (Fig. 4b). Such measurement allows to directly link the rectangular periodic pattern with the detection of the larger Mo and Cl atoms. The extracted in-plane unit cell parameters $a = 4.3 \text{ \AA}$ and $b = 7.1 \text{ \AA}$ match well with the predicted values⁴⁸ (see Supplementary Note 4).

Knowing the crystal axis orientation, to obtain a quantitative evaluation of the optical anisotropy, we take reflectivity spectra of the exfoliated flakes (see Methods section). We filter the illumination source with a polarizer rotated parallel, $|x\rangle$, or perpendicular, $|y\rangle$, to the short flake edge corresponding to the [100] crystal axis. The $|x\rangle$ -polarized reflectivity (Fig. 4c, yellow curve) is consistent with a metallic response close to the plasma frequency, where the reflectivity decreases as the theoretically predicted ϵ_x increases (Supplementary Fig. 2). The drop in reflectivity below 600 nm explains the yellow colour of the flake, as observed in Fig. 4a (left panel). The spectrum along $|y\rangle$ (Fig. 4c, green curve) shows instead oscillations associated with multiple reflections in the Fabry-Perot cavity formed by the flake, which behaves as a low-loss dielectric slab (with thickness 560 nm for the measurement shown in Fig. 4c) along the [010] direction.

The experimental verification of the hyperbolic PPs in MoOCl₂ thin-films requires a near-field excitation and detection scheme. As for the excitation, we fabricate a gold disk on the flake surface (see Methods). Scattering of illuminating light from the disk provides wavevectors beyond the free-space light cone that can couple to the polaritonic modes of the material. For the detection instead, we use a scattering-type scanning near-field optical microscope (s-SNOM) which allows the subwavelength imaging of modes with large in-plane momenta (see Methods)^{17,22,23,46,53}.

Near-field amplitude maps obtained on a 42 nm-thick flake at $\lambda_0 = 830, 730, 633$ and 532 nm are shown in Fig. 4d–g (the yellow circle indicates the position of the disk). At 830 nm and 730 nm (Fig. 4d, e), we observe hyperbolic wavefronts coming from PPs launched by the gold disk. The asymmetry observed in the oscillations on different sides of the launcher (i.e., left-right sides) is due to the opposite sign of the polariton wavevector with respect to the one of the excitation beams (see Supplementary Note 7)⁴⁶. A small misalignment in the illumination relative to the [100] axis is likely the main contribution to the slight asymmetry between the upper and lower fringes. At 633 nm (Fig. 4f), we observe the coexistence of the hyperbolic and lenticular-like modes, as evidenced by the presence of broad, directional wavefronts with a hyperbolic interference (see Supplementary Note 2). The presence of hyperbolic PPs is also highlighted by the ray-like propagation on the right-side of the disk (Fig. 4d–f). At 532 nm (Fig. 4g), we only observe the directional propagation from the lenticular IFC as the hyperbolic mode lies at very high wavevectors that are not efficiently excited in our

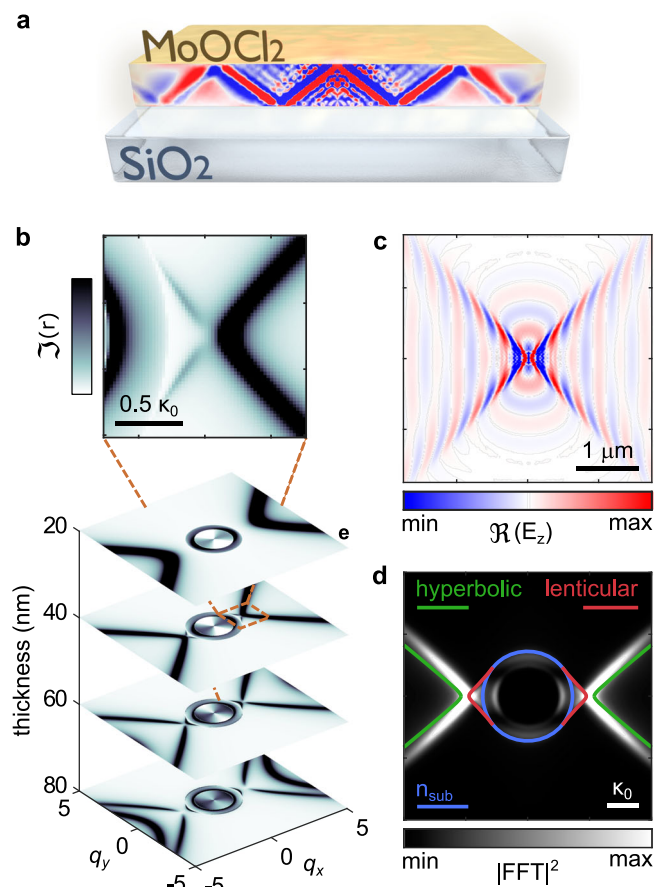


Fig. 3 | Plasmon Polaritons propagation in MoOCl₂ thin-films. **a** Schematic representation of PPs in a thin MoOCl₂ film on a SiO₂ substrate propagating in a ray-light fashion and getting reflected at the top/bottom interfaces. **b** In-plane polariton dispersion calculated with the transfer matrix method for different film thicknesses. Inset: zoom view of the intersection between hyperbolic and lenticular modes for a 40 nm MoOCl₂. $\kappa_0 = 2\pi/\lambda_0$ is the free-space light wavevector. **c** Simulated $\text{Re}(E_z)$ of PPs launched by a near-field source positioned on a 40 nm MoOCl₂ film and **d** corresponding square modulus of the (fast-)Fourier transform (FFT) map. Solid lines represent analytical calculations. Hyperbolic PPs are marked in green and lenticular modes in red. Blue line indicates the substrate light-cone at $|\mathbf{q}| = n_{\text{sub}}$, where n_{sub} is the substrate refractive index.

experiment (the momentum imparted by the near-field source depends on its physical dimensions⁴⁶, see Supplementary Note 8).

In Fig. 4h–k we show the FFT maps computed from the experimental data in Fig. 4d–g (see Supplementary Note 7) together with the theoretical dispersions calculated in the thin-film limit. We indicate with green, red, and blue lines the hyperbolic, lenticular, and substrate (circle with radius $n_{\text{sub}} = 1.5$) modes, respectively. We obtain very good agreement with the theoretical dispersion for the long wavelength maps (Fig. 4h, i), confirming the presence of hyperbolic PPs in MoOCl₂ flakes. For smaller values of λ_0 (Fig. 4j, k), the FFT maps show the presence of the lenticular mode branching from the n_{sub} circle. Here, the agreement with theory diminishes as the thin-film approximation tends to overestimate the polariton momentum (see Supplementary Note 2).

From the experimental maps, we extract the PPs propagation length by fitting the oscillations profiles with an exponentially damped sinusoid⁵³ along tilted lines following the hyperbolic propagation, marked by the dashed arrow in Fig. 4d (see Supplementary Note 9). From the fit, we compute the polariton quality factor Q_p (see Supplementary Note 9) reported in Fig. 4l and estimate a value for the PPs

lifetime τ_p on the order of hundreds of fs (see Supplementary Note 9). Strikingly, while PPs are generally regarded to be lossy, the extracted Q_p are comparable with values reported for PhPs in calcite⁵³, hBN⁵⁴, and MoO₃⁵⁵.

From the s-SNOM data we also extract the hyperbolic rays' opening angle $2\alpha_H$, as shown in Fig. 4d. We exclude here the 532 nm map, as we do not observe hyperbolic PPs at this frequency (Fig. 4g). The extracted data follow the theoretically predicted trend^{17,19} determined by $\alpha_H = (\pi/2 - \tan^{-1} \sqrt{-\epsilon_x/\epsilon_y})$ (Fig. 4m, see also Supplementary Note 2). This is in line with the increase of the angular aperture of the asymptotes ($\pi/2 - \alpha_H$) of the IFCs when increasing λ_0 (see discussion above and Supplementary Note 2). The experimental values are <10% off the predicted values and overlap with the DFT-based⁴⁸ theoretical prediction within the associated error (see Supplementary Note 9).

To enrich our observations, we measure the PPs from the edge of a 20 nm-thick crystal along the metallic direction ([100]) for different wavelengths. Since these PPs are tip-launched (see Supplementary Note 10), the observed periodicity is unaffected by the illumination geometry, hence there are no additional uncertainties in retrieving the PPs momentum (differently from the edge-launched PPs from the gold disk, see Supplementary Note 7)⁵⁶. When comparing the reconstructed dispersion relation with the results obtained from the transfer matrix method, the experimental values appear shifted towards $\sim 10\%$ higher momenta, still preserving the overall trend and overlapping with the theoretical value within the experimental error (Fig. 4n and Supplementary Note 10).

Even if the presented data are in line with our theoretical analysis, the slight discrepancies reported in Fig. 4m, n suggest that the dielectric permittivity of MoOCl₂ might differ from the DFT calculations of ref. 48. Indeed, in both the experimental datasets, the shift could be explained by an actual larger permittivity along the [100] direction in the considered wavelength range. A possible physical justification can be a modification of the actual dielectric response of the material due to electronic correlation effects, not considered in the DFT computations, as suggested in ref. 57.

Discussion

We demonstrated by real-space nanoimaging that MoOCl₂ crystals host propagating polaritons with hyperbolic contours at near-IR and visible frequencies. Leveraging PPs instead of PhPs is the key element enabling the increase in the operation frequency. While anisotropic PPs have been investigated before, they had only been observed at terahertz frequencies⁵⁸ or in the mid-IR upon ultrafast excitation⁵⁹. Our findings extend the control over nanoscale light propagation achieved by PhPs in the mid-IR to the technologically relevant visible range. As MoOCl₂ is stable in air without the need of any protection layer, it constitutes an ideal platform to realize applications of hyperbolic materials that until now lacked widespread implementation due to the combination of high losses in metals and limited fabrication resolution in metamaterials.

Besides the presence of hyperbolic polaritons, we believe the unique properties of MoOCl₂ can be leveraged for several nanophotonic applications in the visible spectrum. For example, in-plane anisotropic media have recently attracted considerable attention for the realization of ultra-compact optical elements for polarization manipulation^{60,61}. While several materials show good optical dichroism (i.e., difference in the refractive index imaginary part) at the expense of large losses or low absolute transmission/reflection, MoOCl₂ features a wide low-loss frequency range with both large optical dichroism and birefringence⁶², making it a good candidate for the realization of ultra-compact optical elements with low dissipation. Moreover, thanks to its metallic character with low electron density, MoOCl₂ is a promising candidate for optical devices reconfigurable through electrostatic gating, providing an easily accessible alternative to percolated ultra-thin metallic films⁶³.

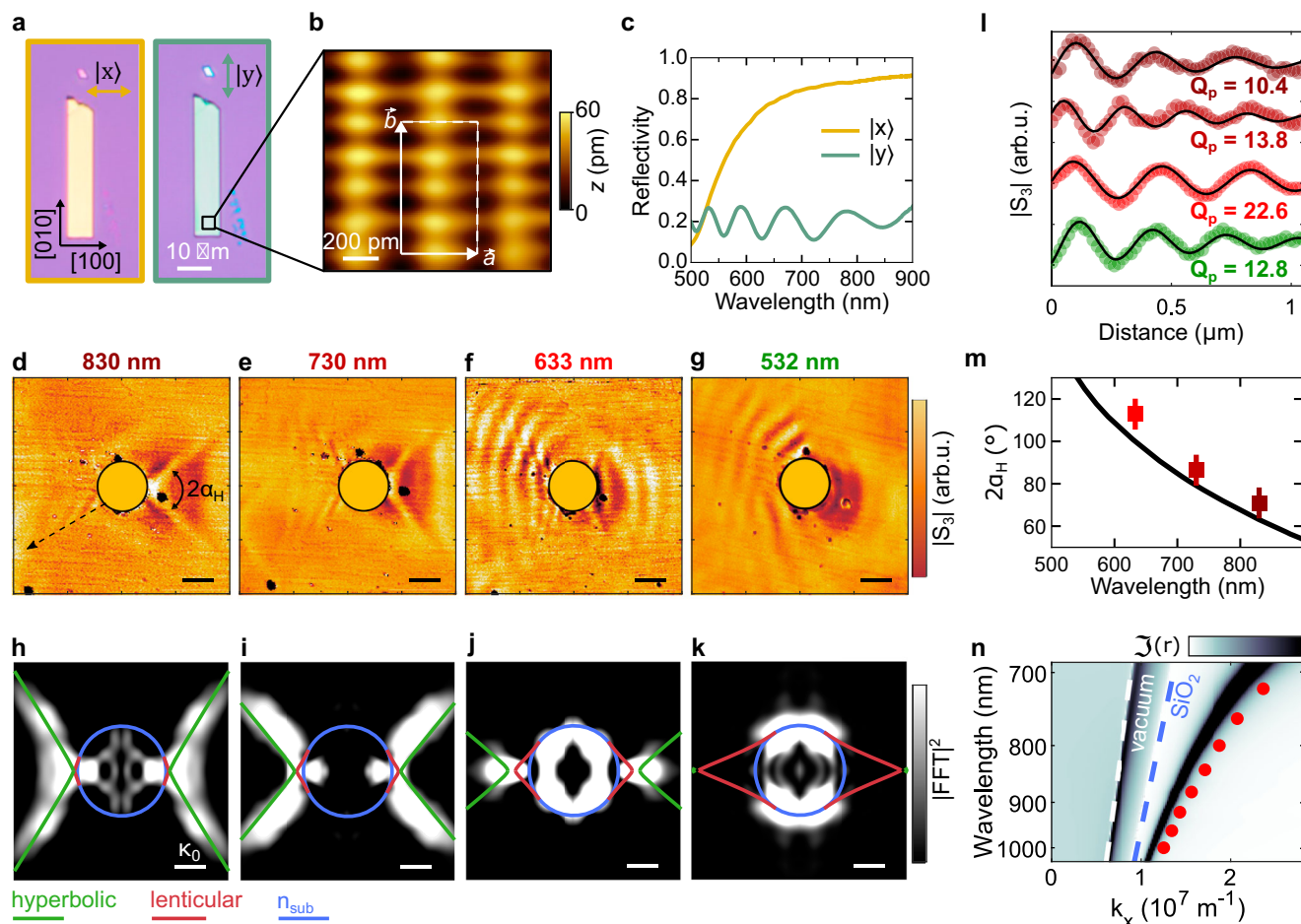


Fig. 4 | Characterization of MoOCl₂ anisotropy and real-space imaging of hyperbolic PPs at visible and near-IR frequencies. **a** Optical images of an as-exfoliated flake with illumination polarized along the $|x\rangle$ (left) and $|y\rangle$ (right) directions. **b** High resolution atomic force microscopy (AFM) of the flake surface, where in-plane crystal unit cell vectors are indicated by white arrows. **c** Reflectivity spectra obtained with a polarized source along the $|x\rangle$ (yellow) and $|y\rangle$ (green) directions of a thick flake (~ 560 nm). **d–g** s-SNOM amplitude maps (third demodulation order) of PPs launched by a gold disk (yellow circle) fabricated on top of the flake (thickness 42 nm) at $\lambda_0 = 830, 730, 633$ and 532 nm (scale bars: 500 nm). $2\alpha_H$ indicates the opening angle of hyperbolic PPs. **h–k** Corresponding FFT maps with superimposed analytical results of the PPs dispersion in the thin-film

approximation (blue: SiO₂ light-cone; red: lenticular modes; green: hyperbolic modes). **l** PPs decay extracted along the hyperbolic profiles as shown by dashed line in **(d)**. Solid lines: best-fits of the profiles allowing for the extraction of the decay length and polariton quality factor Q_p . **m** Aperture angle $2\alpha_H$ of the hyperbolic PPs extracted from the experiments as shown in **(d)**. Black curve corresponds to theoretical predictions. Error bars are evaluated from the width of the fringes in the direction perpendicular to the PPs propagation. **n** Experimental dispersion relation of PPs along the metallic direction of a 20 nm flake (red dots) superimposed to the transfer matrix calculations. The white (blue) dashed line corresponds to the light-line in air (in the SiO₂ substrate).

MoOCl₂ is a natural, air-stable vdW material with a plasma frequency in the visible, representing a unique metallic platform for the emerging field of all-vdW nanophotonics^{64,65} which, until now, could only operate with dielectric elements at visible frequencies. Given all the unique properties mentioned above, MoOCl₂ could be potentially leveraged to realize high-frequency tunable miniaturized polarization elements⁶⁶ and metasurfaces⁶⁷.

Methods

Electromagnetic full-wave simulations

Electromagnetic simulations were performed with a commercial solver (CST Studio) in frequency domain. The dielectric function of MoOCl₂ was taken from theoretical calculations in ref. 48 and modelled as an anisotropic media in CST. We placed a dipole-like near-field source immersed in the middle of a slab of MoOCl₂ to excite all the PPs modes with high wavevectors beyond the free-space light momentum κ_0 ²⁶. The near-field source was obtained by inserting a discrete port in a vacuum gap inside a perfect conducting cylinder with rounded caps (see Supplementary Note 8). As CST does not support open

boundaries for anisotropic media, a vacuum gap was inserted between the end of the MoOCl₂ slab and the open boundary conditions. As port modes touching anisotropic media are also not supported, the near-field source in the simulations shown in Fig. 2c, d was placed in a small vacuum enclosure in the middle of the MoOCl₂ slab.

Transfer matrix technique

The calculations of the imaginary part of the reflection coefficients were performed using a 4×4 transfer matrix formalism⁶⁸ for a stack of homogenous media with arbitrary anisotropic dielectric tensor. The two-dimensional maps in Fig. 3b were obtained by rotating the MoOCl₂ dielectric function around the z -axis and computing the reflection coefficients at each angle.

Mechanical Exfoliation

Two different substrates were used: fused silicon oxide (SiO₂) and boron-doped Si wafer with 285 nm of thermally grown SiO₂ on top (SiO₂/Si), both purchased (Wafer University). Before the exfoliation, the substrates were soaked for 5 minutes in acetone to remove organic

residues and rinsed with isopropyl alcohol (IPA). The thin flakes were exfoliated by the standard mechanical exfoliation method starting from a MoOCl₂ bulk crystal (HQ Graphene), using commercially available processing tape purchased from Ultron Systems, Inc. The exfoliated samples were cleaned with a 30 min bath in N-Methyl-2-Pyrrolidone (NMP) at 80 °C to remove the residues from the exfoliation, then bathed in acetone for 5 min and rinsed with IPA.

Atomic resolution atomic force microscopy

The AFM experiments related to Fig. 4b were performed in air, at room temperature, using a Multimode 8 (Bruker) AFM microscope. ARROW-UHF (NanoAndMore) cantilevers (spring constant $\approx 40 \text{ Nm}^{-1}$) were used as received. The images were obtained in contact mode, with a set-point of about 5 nm. Once the final scan size of about $10 \text{ nm} \times 10 \text{ nm}$ was reached, the scan rate was set to about 20 Hz to minimize the thermal drift and enhance the atomic resolution contrast. The AFM images were analysed with the Gwyddion software (version 2.65). First, the data were levelled by mean plane subtraction and the row alignment tool was applied. The data were then FFT-filtered, and the residual drift was corrected with the Drift Correction tool. The measurements of the lattice constants were extracted with the Lattice tool in the software. Unfiltered data are shown in Supplementary Fig. 14 in Supplementary Note 4.

Far-field optical characterization

The images shown in Fig. 4a and Supplementary Figs. 12, 13 in the Supplementary Information were taken in an optical microscope. For the polarized measurements, the incoming light was polarized with a broadband polarizer. No polarizer was put in the collection path. For the cross-polarization measurements (see Supplementary Fig. 12 in the Supplementary Information), a polarizer was added in collection. The reflection measurements shown in Fig. 4c were taken by placing samples in an inverted microscope (Nikon Eclipse Ti2) coupled to an optical spectrometer (Andor Kymera 328) equipped with a wide range grating (150 lines/mm) and an electrically cooled CCD (Andor Newton). A supercontinuum laser (SuperK Extreme by NKT Photonics) was employed as illumination source. The incoming light was polarized with a wire-grid polarizer (ThorLabs). The samples were exfoliated on SiO₂ to minimize the optical contribution of the substrate. All the measurements were normalized to the reflection of a silver mirror measured in the same illumination condition.

Fabrication of the gold antennas

The antennas used in the near-field experiments were fabricated by means of electron beam lithography on flakes exfoliated on SiO₂/Si substrates. The sample was spin-coated with an e-beam positive resist (PMMA 950k) for 1 min at 4000 rpm and baked on a hot plate for 3 min at 160 °C to remove the solvents. After the lithography, the resist was developed by soaking the sample for 1 min in a solution 1:3 of (Methyl Isobutyl Ketone):IPA at room temperature. 5 nm of chromium (used as adhesive layer), followed by 45 nm of high-purity gold were then deposited in high vacuum in a thermal evaporator. The sample was left in acetone overnight to lift off the resist mask and then cleaned with a 30 min bath in NMP at 80 °C. Finally, the sample was bathed in acetone and rinsed with IPA. For more details, see Supplementary Note 6.

Scattering scanning near-field optical microscopy

Near-field maps of Fig. 4d–g were obtained with a commercial s-SNOM set-up (Neaspec). Briefly, a laser beam is focused by an off-axis parabolic mirror under the apex of a metal-coated (Pt/Ir) AFM tip (with polarization along the tip elongated axis) operating in tapping mode (tapping amplitude $\approx 50 \text{ nm}$) over the sample (gold disk on MoOCl₂), which is raster scanned below the tip, and the backscattered signal is collected by the same parabolic mirror and sent to the detector. The tip acts as a moving near-field source itself, providing the required

momenta to launch PPs. The modes launched by the tip are scattered by the gold disk or vice versa. A modulated far-field signal at the detector plane results from the interference of the light scattered from the tip and the disk. This modulation is a function of the tip-disk distance and results in the imaging of the propagating modes. To isolate the near field component, the signal is demodulated at higher harmonics ($n\Omega, n=3$) of the cantilever oscillation frequency ($\Omega \approx 280 \text{ kHz}$). Before focusing, half of the light is redirected towards a pseudo-heterodyne interferometer by a beam splitter. The light scattered by the tip is then recombined with the interferometer reference to retrieve amplitude and phase resolved maps of the electromagnetic field at the sample surface. To optimize the PPs scattering, we rotate the MoOCl₂ flake so that the [100] axis is aligned with the laser incident direction (horizontal direction in Fig. 4d–g). The light sources used in the experiments are a Titanium-Sapphire laser covering the 700–1000 nm range (SolsTiS, M2), a 633 nm diode laser (Match Box, Integrated Optics), and a 532 nm diode laser (LCX-532, Oxixius). All the measurements were done in air and at room temperature.

Data availability

The Source Data underlying Fig. 4 (reflectivity, atomic resolution map and s-SNOM images) can be accessed at <https://doi.org/10.5281/zenodo.13993338>. Additional data are available from the corresponding authors upon request.

Code availability

Codes supporting the results of this work are available from the corresponding authors upon request.

References

1. Basov, D. N., Fogler, M. M. & García De Abajo, F. J. Polaritons in van der Waals materials. *Science* **354**, aag1992 (2016).
2. Hirsch, L. R. et al. Nanoshell-mediated near-infrared thermal therapy of tumors under magnetic resonance guidance. *Proc. Natl Acad. Sci. USA* **100**, 13549–13554 (2003).
3. Baffou, G., Cichos, F. & Quidant, R. Applications and challenges of thermoplasmonics. *Nat. Mater.* **19**, 946–958 (2020).
4. Cortés, E. et al. Challenges in plasmonic catalysis. *ACS Nano* **14**, 16202–16219 (2020).
5. Herran, M. et al. Plasmonic bimetallic two-dimensional supercrystals for H₂ generation. *Nat. Catal.* **6**, 1205–1214 (2023).
6. Xu, Y. et al. Optical refractive index sensors with plasmonic and photonic structures: promising and inconvenient truth. *Adv. Opt. Mater.* **7**, 1801433 (2019).
7. Langer, J. et al. Present and future of surface-enhanced Raman scattering. *ACS Nano* **14**, 28–117 (2020).
8. Yu, N. et al. Light propagation with phase discontinuities: generalized laws of reflection and refraction. *Science* **334**, 333–7 (2011).
9. Genevet, P. et al. Controlled steering of Cherenkov surface plasmon wakes with a one-dimensional metamaterial. *Nat. Nanotechnol.* **10**, 804–809 (2015).
10. Wintz, D., Ambrosio, A., Zhu, A. Y., Genevet, P. & Capasso, F. Anisotropic surface plasmon polariton generation using bimodal V-antenna based metastructures. *ACS Photonics* **4**, 22–27 (2017).
11. Lee, J. et al. Giant nonlinear response from plasmonic metasurfaces coupled to intersubband transitions. *Nature* **511**, 65–69 (2014).
12. Mesch, M., Metzger, B., Hentschel, M., & Giessen, H. Nonlinear plasmonic sensing. *Nano Lett.* **16**, 3155–3159 (2016).
13. Wang, H. et al. Planar hyperbolic polaritons in 2D van der Waals materials. *Nat. Commun.* **15**, 1–14 (2024).
14. Poddubny, A., Iorsh, I., Belov, P. & Kivshar, Y. Hyperbolic metamaterials. *Nat. Photonics* **7**, 948–957 (2013).
15. Galiffi, E. et al. Extreme light confinement and control in low-symmetry phonon-polaritonic crystals. *Nat. Rev. Mater.* **9**, 9–28 (2023).

16. Tamagnone, M. et al. Ultra-confined mid-infrared resonant phonon polaritons in van der Waals nanostructures. *Sci. Adv.* **4**, eaat7189 (2018).
17. Dai, S. et al. Tunable phonon polaritons in atomically thin van der Waals crystals of boron nitride. *Science* **343**, 1125–1129 (2014).
18. Ambrosio, A. et al. Selective excitation and imaging of ultraslow phonon polaritons in thin hexagonal boron nitride crystals. *Light Sci. Appl.* **7**, 27 (2018).
19. Li, P. et al. Hyperbolic phonon-polaritons in boron nitride for near-field optical imaging and focusing. *Nat. Commun.* **6**, 1–9 (2015).
20. Ambrosio, A. et al. Mechanical detection and imaging of hyperbolic phonon polaritons in hexagonal boron nitride. *ACS Nano* **11**, 8741–8746 (2017).
21. Chaudhary, K. et al. Engineering phonon polaritons in van der Waals heterostructures to enhance in-plane optical anisotropy. *Sci. Adv.* **5**, eaau7171 (2019).
22. Zheng, Z. et al. A mid-infrared biaxial hyperbolic van der Waals crystal. *Sci. Adv.* **5**, eaav8690 (2019).
23. Ma, W. et al. In-plane anisotropic and ultra-low-loss polaritons in a natural van der Waals crystal. *Nature* **562**, 557–562 (2018).
24. Passler, N. C. et al. Hyperbolic shear polaritons in low-symmetry crystals. *Nature* **602**, 595–600 (2022).
25. Matson, J. et al. Controlling the propagation asymmetry of hyperbolic shear polaritons in beta-gallium oxide. *Nat. Commun.* **14**, 1–8 (2023).
26. Zhang, Q. et al. Unidirectionally excited phonon polaritons in high-symmetry orthorhombic crystals. *Sci. Adv.* **8**, eabn9774 (2022).
27. Hu, G. et al. Topological polaritons and photonic magic angles in twisted α -MoO₃ bilayers. *Nature* **582**, 209–213 (2020).
28. Álvarez-Pérez, G. et al. Negative reflection of nanoscale-confined polaritons in a low-loss natural medium. *Sci. Adv.* **8**, 8486 (2022).
29. Sternbach, A. J. et al. Negative refraction in hyperbolic heterobichystals. *Science* **379**, 555–557 (2023).
30. Wu, X. & Fu, C. Near-field radiative heat transfer between uniaxial hyperbolic media: role of volume and surface phonon polaritons. *J. Quant. Spectrosc. Radiat. Transf.* **258**, 107337 (2021).
31. Bylinkin, A. et al. Real-space observation of vibrational strong coupling between propagating phonon polaritons and organic molecules. *Nat. Photonics* **15**, 197–202 (2021).
32. Liu, Z., Lee, H., Xiong, Y., Sun, C. & Zhang, X. Far-field optical hyperlens magnifying sub-diffraction-limited objects. *Science* **315**, 1686 (2007).
33. Jacob, Z. et al. Active hyperbolic metamaterials: enhanced spontaneous emission and light extraction. *Optica* **2**, 62–65 (2015).
34. Lee, Y. U. et al. Hyperbolic material enhanced scattering nanoscopy for label-free super-resolution imaging. *Nat. Commun.* **13**, 1–8 (2022).
35. Sun, J. & Litchinitser, N. M. Toward practical, subwavelength, visible-light photolithography with hyperlens. *ACS Nano* **12**, 542–548 (2018).
36. High, A. A. et al. Visible-frequency hyperbolic metasurface. *Nature* **522**, 192–196 (2015).
37. Lee, D. et al. Realization of wafer-scale hyperlens device for sub-diffractive biomolecular imaging. *ACS Photonics* **5**, 2549–2554 (2018).
38. Kang, E. S. H. et al. Organic anisotropic excitonic optical nanoantennas. *Adv. Sci.* **9**, 2201907 (2022).
39. Lee, Y. U., Yim, K., Bopp, S. E., Zhao, J. & Liu, Z. Low-loss organic hyperbolic materials in the visible spectral range: a joint experimental and first-principles study. *Adv. Mater.* **32**, 2002387 (2020).
40. Esslinger, M. et al. Tetradymites as natural hyperbolic materials for the near-infrared to visible. *ACS Photonics* **1**, 1285–1289 (2014).
41. Córdova-Castro, R. M. et al. Anisotropic plasmonic CuS nanocrystals as a natural electronic material with hyperbolic optical dispersion. *ACS Nano* **13**, 6550–6560 (2019).
42. Shao, Y. et al. Infrared plasmons propagate through a hyperbolic nodal metal. *Sci. Adv.* **8**, 6169 (2022).
43. Korzeb, K. et al. Compendium of natural hyperbolic materials. *Opt. Express* **23**, 25406–25424 (2015).
44. Gjerding, M. N., Petersen, R., Pedersen, T. G., Mortensen, N. A. & Thygesen, K. S. Layered van der Waals crystals with hyperbolic light dispersion. *Nat. Commun.* **8**, 1–8 (2017).
45. Ruta, F. et al. Hyperbolic exciton polaritons in a van der Waals magnet. *Nat. Commun.* **14**, 8261 (2023).
46. Ma, W. et al. Ghost hyperbolic surface polaritons in bulk anisotropic crystals. *Nature* **596**, 362–366 (2021).
47. Gao, H., Ding, C., Sun, L., Ma, X. & Zhao, M. Robust broadband directional plasmons in a MoOCl₂ monolayer. *Phys. Rev. B* **104**, 205424 (2021).
48. Zhao, J. et al. Highly anisotropic two-dimensional metal in monolayer MoOCl₂. *Phys. Rev. B* **102**, 245419 (2020).
49. Wang, Z. et al. Fermi liquid behavior and colossal magnetoresistance in layered MoOCl₂. *Phys. Rev. Mater.* **4**, 041001(R) (2020).
50. Álvarez-Pérez, G., Voronin, K. V., Volkov, V. S., Alonso-González, P. & Nikitin, A. Y. Analytical approximations for the dispersion of electromagnetic modes in slabs of biaxial crystals. *Phys. Rev. B* **100**, 235408 (2019).
51. Narimanov, E. E. Dyakonov waves in biaxial anisotropic crystals. *Phys. Rev. A* **98**, 013818 (2018).
52. Simovski, C. & Tretyakov, S. *An Introduction to Metamaterials and Nanophotonics*. (Cambridge University Press, Cambridge, 2020).
53. Ni, X. et al. Observation of directional leaky polaritons at anisotropic crystal interfaces. *Nat. Commun.* **14**, 2845 (2023).
54. Giles, A. J. et al. Ultralow-loss polaritons in isotopically pure boron nitride. *Nat. Mater.* **17**, 134–139 (2017).
55. Menabde, S. G. et al. Low-loss anisotropic image polaritons in van der Waals crystal α -MoO₃. *Adv. Opt. Mater.* **10**, 2201492 (2022).
56. Kaltenecker, K. J. et al. Mono-crystalline gold platelets: a high-quality platform for surface plasmon polaritons. *Nanophotonics* **9**, 509–522 (2020).
57. Ruta, F. L. et al. *Good plasmons in a bad metal*. Preprint at <https://arxiv.org/abs/2406.05703> (2024).
58. Chen, S. et al. Real-space observation of ultraconfined in-plane anisotropic acoustic terahertz plasmon polaritons. *Nat. Mater.* **22**, 860–866 (2023).
59. Fu, R. et al. Manipulating hyperbolic transient plasmons in a layered semiconductor. *Nat. Commun.* **15**, 1–8 (2024).
60. Niu, S. et al. Giant optical anisotropy in a quasi-one-dimensional crystal. *Nat. Photonics* **12**, 392–396 (2018).
61. Guo, Q. et al. Colossal in-plane optical anisotropy in a two-dimensional van der Waals crystal. *Nat. Photonics* **1**, 1170–1175 (2024).
62. Zhou, Y. et al. A solution-processable natural crystal with giant optical anisotropy for efficient manipulation of light polarization. *Nat. Photonics* **18**, 922–927 (2024).
63. Maniyara, R. A. et al. Tunable plasmons in ultrathin metal films. *Nat. Photonics* **13**, 328–333 (2019).
64. Meng, Y. et al. Photonic van der Waals integration from 2D materials to 3D nanomembranes. *Nat. Rev. Mater.* **8**, 498–517 (2023).
65. Weber, T. et al. Intrinsic strong light-matter coupling with self-hybridized bound states in the continuum in van der Waals metasurfaces. *Nat. Mater.* **22**, 970–976 (2023).
66. Lynch, J. et al. Gate-tunable optical anisotropy in wafer-scale, aligned carbon nanotube films. *Nature Photonics* **1**, 1176–1184 (2024).
67. Jung, C., Lee, E. & Rho, J. The rise of electrically tunable metasurfaces. *Sci. Adv.* **10**, eado8964 (2024).
68. Paarmann, A. & Passler, N. C. Generalized 4 × 4 matrix formalism for light propagation in anisotropic stratified media: study of surface

phonon polaritons in polar dielectric heterostructures. *JOSA B* **34**, 2128–2139 (2017).

Acknowledgements

The authors would like to thank Lin Nan for the help with the 3D rendering of the graphics. The authors would also like to acknowledge Dmitri Basov and Francesco Ruta for the insightful discussion about the interpretation of the experimental data. This work has been financially supported by the European Research Council (ERC) under the European Union Horizon 2020 research and innovation programme 'METAmorphoses', grant agreement no. 817794 (awarded to A.A.).

Author contributions

A.M. conceived the idea. G.V. and N.M. fabricated the samples. N.M. and G.V. performed the far-field measurements. S.C. carried out the atomic force microscopy experiments. G.V. and A.M. performed the near-field measurements. G.V. and A.M. carried out the numerical simulations and theoretical analysis. G.V., A.M., N.M. and A.A. wrote the paper with contributions from all other authors. All the authors discussed the implementation of the research, the experimental data and the related analysis. A.A. coordinated the research activities.

Competing interests

The authors declare no competing interests.

Additional information

Supplementary information The online version contains supplementary material available at <https://doi.org/10.1038/s41467-024-53988-7>.

Correspondence and requests for materials should be addressed to Andrea Mancini or Antonio Ambrosio.

Peer review information *Nature Communications* thanks the anonymous reviewers for their contribution to the peer review of this work. A peer review file is available.

Reprints and permissions information is available at <http://www.nature.com/reprints>

Publisher's note Springer Nature remains neutral with regard to jurisdictional claims in published maps and institutional affiliations.

Open Access This article is licensed under a Creative Commons Attribution-NonCommercial-NoDerivatives 4.0 International License, which permits any non-commercial use, sharing, distribution and reproduction in any medium or format, as long as you give appropriate credit to the original author(s) and the source, provide a link to the Creative Commons licence, and indicate if you modified the licensed material. You do not have permission under this licence to share adapted material derived from this article or parts of it. The images or other third party material in this article are included in the article's Creative Commons licence, unless indicated otherwise in a credit line to the material. If material is not included in the article's Creative Commons licence and your intended use is not permitted by statutory regulation or exceeds the permitted use, you will need to obtain permission directly from the copyright holder. To view a copy of this licence, visit <http://creativecommons.org/licenses/by-nc-nd/4.0/>.

© The Author(s) 2024